ACS OMEGA

http://pubs.acs.org/journal/acsodf

Article

Syntheses, Structures, and Properties of Coordination Polymers with 2,5-Dihydroxy-1,4-Benzoquinone and 4,4′-Bipyridyl Synthesized by *In Situ* Hydrolysis Method

Daiki Yamazui, Kaiji Uchida, Shohei Koyama, Bin Wu, Hiroaki Iguchi, Wataru Kosaka, Hitoshi Miyasaka, and Shinya Takaishi*

Cite This: *ACS Omega* 2022, 7, 18259−18266

Read Online

ACCESS | Metrics & More | Article Recommendations | Supporting Information

ABSTRACT: The coordination polymers (CPs) with binary ligands, including 2,5-dihydroxy-1,4-benzoquinone (H2DHBQ) and 4,4′-bipyridyl (bpy), were synthesized using *in situ* hydrolysis of 2,5-dimethoxy-1,4-benzoquinone (DMBQ). Three kinds of CPs were obtained depending on the metal ions. For M = Mn and Zn, a 1D zigzag chain structure with cis conformation (***cis*-1D-M**) was obtained, whereas Co, Ni, and Cu compounds afforded a 2D net structure with trans conformation (**trans-2D-M**) with a 1D pore. A linear chain structure was also obtained for M = Cu. Magnetic susceptibility ($\chi_M T$) at 300 K in ***cis*-1D-Mn** and ***trans*-2D-Co** was evaluated to be 4.421 and 2.950 cm^3 K mol^{-1}, respectively, indicating that both compounds are in the high-spin state. According to the N_2 adsorption isotherms at 77 K, ***trans*-2D-Ni** showed microporosity with the BET surface area of 177 m^2 g^{-1}, whereas the isomorphic ***trans*-2D-Co** rarely adsorbed N_2 at 77 K. This phenomenon was explained by the difference of diffusion kinetics of the adsorbent molecules, which was supported by the CO_2 adsorption isotherms at 195 K. The optical band gaps of ***cis*-1D-Mn**, ***cis*-1D-Zn**, ***trans*-2D-Co**, and ***trans*-2D-Ni** were estimated to be 1.6, 1.8, 1.0, and 1.1 eV, respectively, by using UV−vis−NIR spectroscopy.

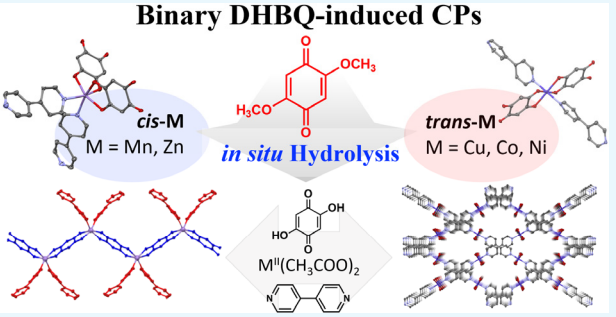

INTRODUCTION

Coordination polymers (CPs) with a permanent porosity, including metal−organic frameworks (MOFs), have attracted attention as molecular porous materials because of their potential applications for gas storage,[1−7] gas separation,[8−11] sensing,[12] catalysis,[13−15] etc. In particular, redox-active CPs have been gaining a lot of interest because of their marked electronic properties. 2,5-Dihydroxy-1,4-benzoquinone (H2DHBQ, R = H in Figure 1) and its derivatives are widely used as a redox-active ligand for CP syntheses, and remarkable magnetic[16−18] and conductive[19−21] properties have been reported. Though various structural motifs such as 1D chain,[22] 2D honeycomb sheet,[16−21] and 3D (10,3)-*a* net[23] have been reported using DHBQ and its derivatives, more structural diversity is required for further study of these CPs. One useful approach to afford structural diversity is to introduce auxiliary ligands. To date, no reports of DHBQ-based CPs have been reported with binary ligands, although some reports exist for chloranilic acid (R = Cl).[24−26] A plausible reason for this is due to the fast complexation of DHBQ ligand, which makes it difficult to obtain the phase-pure product or to obtain single crystals. *In situ* generation of the active ligand is a useful way to control the speed of crystallization. Abrahams and co-workers reported several single crystals of DHBQ-based CPs by using *in situ* generation of DHBQ by hydrolysis of 2,5-diamino-1,4-benzoquinone (DABQ).[23] Recently, such an *in situ* generation of the active

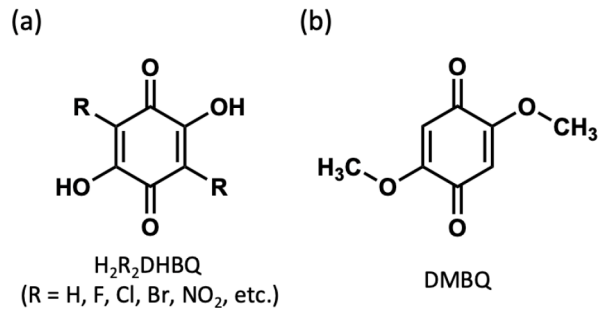

Figure 1. Molecular structures of (a) H_2DHBQ derivatives and (b) DMBQ.

Received: December 16, 2021
Accepted: May 16, 2022
Published: May 24, 2022

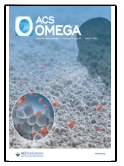

ligand has also been used for introduction of functional groups in the CPs.[27,28] Herein, we utilized the *in situ* synthesis for introduction of the auxiliary ligands by using 2,5-dimethoxy-1,4-benzoquinone (DMBQ, Figure 1) as a precursor of DHBQ. Using this method, we obtained three kinds of the structural motifs of binary CPs with DHBQ and 4,4′-bipyridyl (bpy), which are a 1D zigzag chain of *cis*-$[M(DHBQ)(bpy)_2]$ for M = Mn and Zn (***cis*-1D-M**), a 3D porous framework composed of an interlocked 2D rectangular net of *trans*-$[M(DHBQ)(bpy)]\cdot n(H_2O)$ for M = Co, Cu, and Ni (***trans*-2D-M**), and a 1D linear chain of *trans*-$[M(DHBQ)(bpy)_2]$ for M = Cu (***trans*-1D-M**). In this paper, we report their structure, thermogravimetry, spectroscopic properties, and porosity.

EXPERIMENTAL SECTION

Characterization and Instrumental Procedures. $Mn(OAc)_2\cdot 4H_2O$, $Co(OAc)_2\cdot 4H_2O$, $Ni(OAc)_2\cdot 4H_2O$, $Cu(OAc)_2\cdot H_2O$, and $Zn(OAc)_2\cdot 2H_2O$ were purchased from Fujifilm Wako Chemicals and used as received. 2,5-Dihydroxy-1,4-benzoquionone (H_2DHBQ) was purchased from Acros Organics and used as received. 4,4′-Bipyridyl (bpy) was purchased from TCI chemicals and used as received.

Solid-state IR spectra from 600 to 4000 cm^{-1} were collected on a JASCO FT/IR 4200 Fourier transform infrared spectrometer by means of an attenuated total reflection (ATR) method with 4 cm^{-1} resolution. Solid-state UV−vis−NIR spectra from a diffuse reflection method were recorded on a Shimadzu UV-3100. Samples were diluted with $BaSO_4$, and obtained diffuse reflectivity spectra were converted to absorption spectra using the Kubelka−Munk function. ^{1}H NMR measurements were performed on a Bruker AV500 at RT. Thermogravimetry (TG) was measured on a SHIMADZU DTG-60/60H at a heating rate of 5 °C/min under a constant nitrogen flow (0.1 L/min). The N_2, H_2, and CO_2 sorption isotherms were measured using MicrotracBEL BELSORP MAX. Density functional theory (DFT) calculations were performed using Gaussian16 software.[29] All geometry optimizations were performed at the UB3LYP/6-31G+(d,p) level of theory.[30−32] Elemental analyses were performed using the J-Science Lab JM-10 equipped in the Research and Analytical Center for Giant Molecules at Tohoku University. Single crystal X-ray crystal structure analyses were performed using a Rigaku Varimax diffractometer with a Mo Kα radiation source. A portion of the single crystals for the crystal structure analysis was directly pipetted from the reaction vials and transferred to a Petri dish. Appropriate single crystals were selected using an optical microscope and then scooped with a MiTeGen crystal mount. The data were collected with an ω-scan strategy under several φ-angles. Data reduction was performed with the CrysAlisPro package, and an empirical absorption correction was applied. The structures were solved by direct methods and refined by full-matrix least-squares on F^2 with anisotropic displacement using the SHELXTL software package.[33] The non-H atoms were treated anisotropically, whereas the hydrogen atoms were placed in calculated, ideal positions and refined as riding on their respective carbon atoms. The electron density in the pore was assigned to oxygen atoms of the water molecules, and their site occupancies were optimized to minimize the R-value. Powder X-ray diffraction (PXRD) patterns for capillary-encapsulated samples were obtained at room temperature with a step of 0.02° using a Rigaku SmartLab diffractometer with Cu Kα radiation source. Magnetic susceptibility at 300 K was measured using Quantum Design MPMS-XL. Scanning electron microscope (SEM) images were acquired using the Hitachi S-4300.

Syntheses. *2,5-Dimethoxy-1,4-Benzoquinone (DMBQ).* DMBQ was prepared following a procedure published earlier.[34] 2,5-Dihydroxy-1,4-benzoquinone (3.3 g, 24 mmol) was stirred in MeOH (850 mL) with 5 mL of 38% HCl (w/w) aq overnight at room temperature. The precipitate was filtered and then purified by recrystallization with N,N-dimethylformamide to obtain a goldish yellow crystalline solid. This crystalline solid was washed with MeOH until the filtrate became colorless and then dried *in vacuo* to afford 3.2 g (81%) of DMBQ. ^{1}H NMR (500 MHz $CDCl_3$) δ 5.87 (s, 2H), δ 3.85 (s, 6H). Found: C, 57.17; H, 4.86; N, 0.00. Calc. for $C_8H_8O_4$: C, 57.18; H, 4.80; N, 0.00.

*cis-Mn(DHBQ)(bpy)$_2$ (**cis-1D-Mn**).* $Mn(OAc)_2\cdot 4H_2O$ (245 mg, 1.0 mmol), finely milled DMBQ (168 mg, 1.0 mmol), and bpy (304 mg, 2.0 mmol) were suspended in 25 mL of deionized water in a 30 mL screw-capped glass vial with a Teflon-coated rubber seal. The suspension was sonicated for several minutes. The vial was put in an electric oven and heated to 120 °C for 24 h. After cooling, the precipitate was collected by filtration. The solid was washed with water, then washed with acetone, and then dried *in vacuo* to obtain a deep brown solid. Yield: 340 mg (67%). Elemental analysis calc. for $C_{26}H_{18}MnN_4O_4$: C, 61.78%; H, 3.60%; N, 11.09%. Found: C, 61.81%; H, 3.77%; N, 10.83%.

*cis-Zn(DHBQ)(bpy)$_2$ (**cis-1D-Zn**).* $Zn(OAc)_2\cdot 2H_2O$ (220 mg, 1.0 mmol), finely milled DMBQ (168 mg, 1.0 mmol), and bpy (304 mg, 2.0 mmol) were suspended in 25 mL of deionized water in a 30 mL screw-capped glass vial with a Teflon-coated rubber seal. The suspension was sonicated for several minutes. The vial was put in an electric oven and heated to 120 °C for 24 h. After cooling, the precipitate was collected by filtration. The solid was washed with water, then washed with acetone, and then dried *in vacuo* to obtain a pink-red solid. Yield: 495 mg (96%). Elemental analysis calc. for $C_{26}H_{18}N_4O_4Zn$: C, 60.53%; H, 3.52%; N, 10.86%. Found: C, 59.87%; H, 3.70%; N, 10.87%.

*trans-Co(DHBQ)(bpy)·2H$_2$O (**trans-2D-Co**).* $Co(OAc)_2\cdot 4H_2O$ (162 mg, 0.65 mmol), finely milled DMBQ (168 mg, 1.0 mmol), and bpy (152 mg, 1.0 mmol) were suspended in 25 mL of deionized water in a 30 mL screw-capped glass vial with a Teflon-coated rubber seal. The suspension was sonicated for several minutes. The vial was put in an electric oven and heated to 120 °C for 24 h. After cooling, the precipitate was collected by filtration. The solid was washed with water, then washed with acetone, and then dried *in vacuo* to obtain a deep brown solid. Yield: 250 mg (99%). Elemental analysis calc. for $C_{16}H_{14}CoN_2O_6$: C, 49.37%; H, 3.63%; N, 7.20. Found: C, 49.48%; H, 3.59%; N, 7.08%.

*trans-Ni(DHBQ)(bpy)·2.25H$_2$O (**trans-2D-Ni**).* $Ni(OAc)_2\cdot 4H_2O$ (249 mg, 1.0 mmol), finely milled DMBQ (168 mg, 1.0 mmol), and bpy (152 mg, 1.0 mmol) were suspended in 25 mL of deionized water in a 30 mL screw-capped glass vial with a Teflon-coated rubber seal. The suspension was sonicated for several minutes. The vial was put in an electric oven and heated to 120 °C for 24 h. After cooling, the precipitate was collected by filtration. The solid was washed with water, then washed with acetone, and then dried *in vacuo* to obtain a red-brown solid. Yield: 375 mg (95%). Elemental analysis calc. for $C_{16}H_{14.50}NiN_2O_{6.25}$: C, 48.8%; H, 3.71%; N, 7.12%. Found: C, 48.99%; H, 3.56%; N, 7.05%.

https://doi.org/10.1021/acsomega.1c07077
ACS Omega 2022, 7, 18259−18266

RESULTS AND DISCUSSION

We synthesized CPs with the existence of metal acetate, DMBQ, and 4,4′-bipyridyl (bpy) under hydrothermal conditions. We obtained several CPs including DHBQ and bpy ligands. When we used manganese and zinc acetate as a metal source, we obtained 1D zigzag chains of *cis*-[M(DHBQ)-(bpy)$_2$] (abbreviated as ***cis*-1D-M**). ***cis*-1D-Mn** and ***cis*-1D-Zn** were isomorphic. The crystal structure of ***cis*-1D-Mn** is shown in Figure 2, and crystallographic parameters are summarized in Table S1. The molar ratio of Mn, DHBQ, and bpy in this compound is 1:1:2. Two $DHBQ^{2-}$ ligands are in cis position and each of them bridges the neighboring Mn^{2+} ions in a bis-bidentate manner, forming a 1D zigzag chain. Two bpy ligands coordinate to the Mn^{2+} in cis position. One nitrogen atom of the bpy ligand coordinates to Mn^{2+}, whereas the other does not interact with any of the neighboring atoms. The distances of Mn−N1, Mn−O1, and Mn−O2 are 2.2487(13), 2.1670(11), and 2.1990(15) Å, respectively. The magnetic susceptibility of ***cis*-1D-Mn** ($\chi_M T$ = 4.421 cm^3 K mol^{-1} at 300 K, namely μ_{eff} = 5.94 μ_B) was similar to the S = 5/2 spin-only value (4.38 cm^3 K mol^{-1}) and that of the representative Mn^{2+} high spin complexes,[35,36] showing that ***cis*-1D-Mn** is in high-spin state. There is a $\pi-\pi$ interaction between $DHBQ^{2-}$ and the neighboring bpy (inter plane distance is 3.454 Å). It should be noted that when we mixed metal acetate, DMBQ, and 4,4′-bipyridyl (bpy) with a 1:1:1 ratio, we obtained the mixture of ***cis*-1D-M** and one-dimensional CP without bpy ligands (M(DHBQ)(H$_2$O)$_2$).[22]

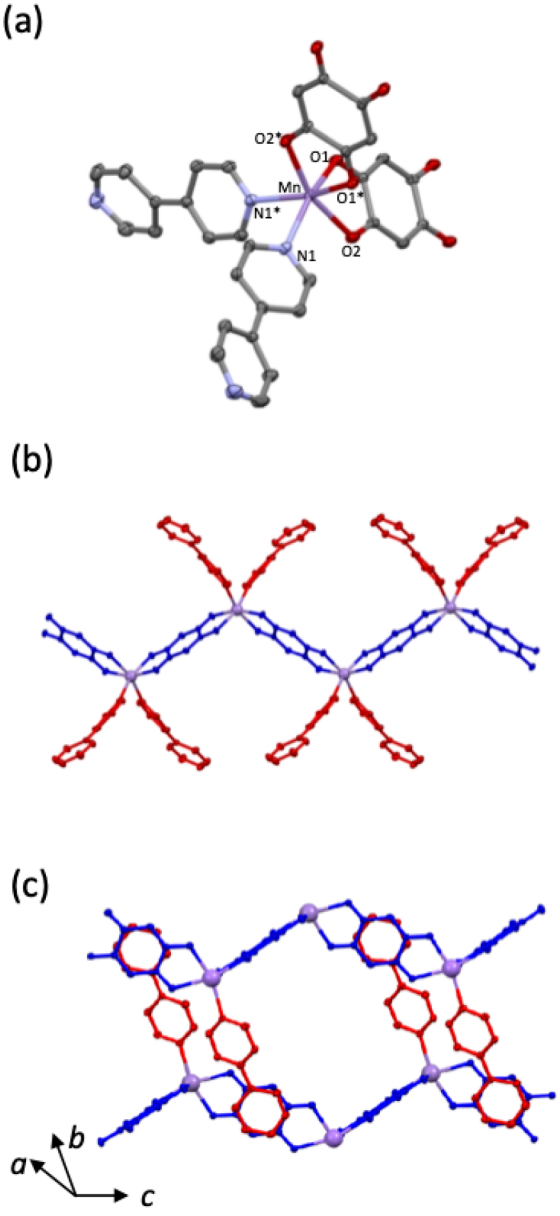

Figure 2. Crystal structure of ***cis*-1D-Mn**. Hydrogen atoms are omitted for clarity. (a) ORTEP drawing of the local environment. (b,c) Two perspective views. DHBQ and bpy are shown in blue and red, respectively.

By mixing cobalt or nickel acetate, DMBQ, and bpy, 2D rectangular nets of *trans*-[M(DHBQ)(bpy)] (***trans*-2D-M**) were obtained. The crystal structure of the Co complex is shown in Figure 3. The crystallographic parameters are summarized in Table S2. The molar ratio of Co, DHBQ, and bpy is 1:1:1, and the DHBQ ligands are in the trans position to form a 1D linear chain (···Co−DHBQ−Co···) along the *c*-axis. In addition, bpy bridges the adjacent 1D chains (···Co−bpy−Co···) along the $a + b$ and $a - b$ directions to form two independent (4,4) rectangular 2D nets, respectively (Figure 3b). Each 2D net interlocked with each other—more specifically, interlocked with parallel−parallel (p−p) mode[37]—to form a polycatenated 3D framework (Figure 3c). There are small 1D pores with ca. 4.2 Å diameter space between two 2D nets (Figure S8). The electron density in the pore was assigned to approximately 2.3 water molecules per formula unit, which is consistent with the elemental analysis. The distances of Co−N1 = 2.142(4) Å and Co−N2* = 2.136(4) Å are longer than that of the four Co−O bond distances [2.057(4), 2.058(4), 2.065(4), and 2.077(4) Å]. Magnetic susceptibility ($\chi_M T$) at 300 K of ***trans*-2D-Co** was 2.950 cm^3 K mol^{-1}, namely μ_{eff} = 4.86 μ_B, which is larger than that expected for the spin-only (1.875 cm^3 K mol^{-1} for S = 3/2 and g = 2.0) but in agreement with the values observed for the octahedral high spin Co^{2+} complexes with a significant first-order orbital contribution.[38] In the case of M = Ni, we concluded that ***trans*-2D-Ni** is isomorphic to ***trans*-2D-Co** according to the PXRD results (Figure 4).

We performed the stability test against the solvents by soaking ***trans*-2D-M** in solvents (H$_2$O, MeOH, EtOH, DMF, CH$_3$CN, and pyridine) for 48 h at room temperature. The PXRD patterns of the compounds before and after soaking are shown in Figure S9. As for the ***trans*-2D-Ni**, the PXRD patterns did not change with soaking for any of the aforementioned solvents, indicating that ***trans*-2D-Ni** has high stability against the solvents and a rigid structure. In the case of ***trans*-2D-Co**, conversely, peak broadening or peak splitting was observed with soaking in DMF, CH$_3$CN, or pyridine, while there was no change in H$_2$O, MeOH, and EtOH. It should be noted that the PXRD patterns returned to original after standing in air for 3 days. Therefore, this change in the PXRD patterns is not due to the collapse of the structure but due to the subtle structural change of the framework by introducing the solvent into the pore. These findings indicate that the framework of the ***trans*-2D-Co** can be more flexible than ***trans*-2D-Ni**, though they are isostructural.

When we used copper acetate as a metal source, the obtained crystalline solid contained two kinds of crystal that could not be visually separated. One is mostly similar with that of ***trans*-2D-Co** (Figure S2 and Table S2), thus we named it

https://doi.org/10.1021/acsomega.1c07077
ACS Omega 2022, 7, 18259−18266

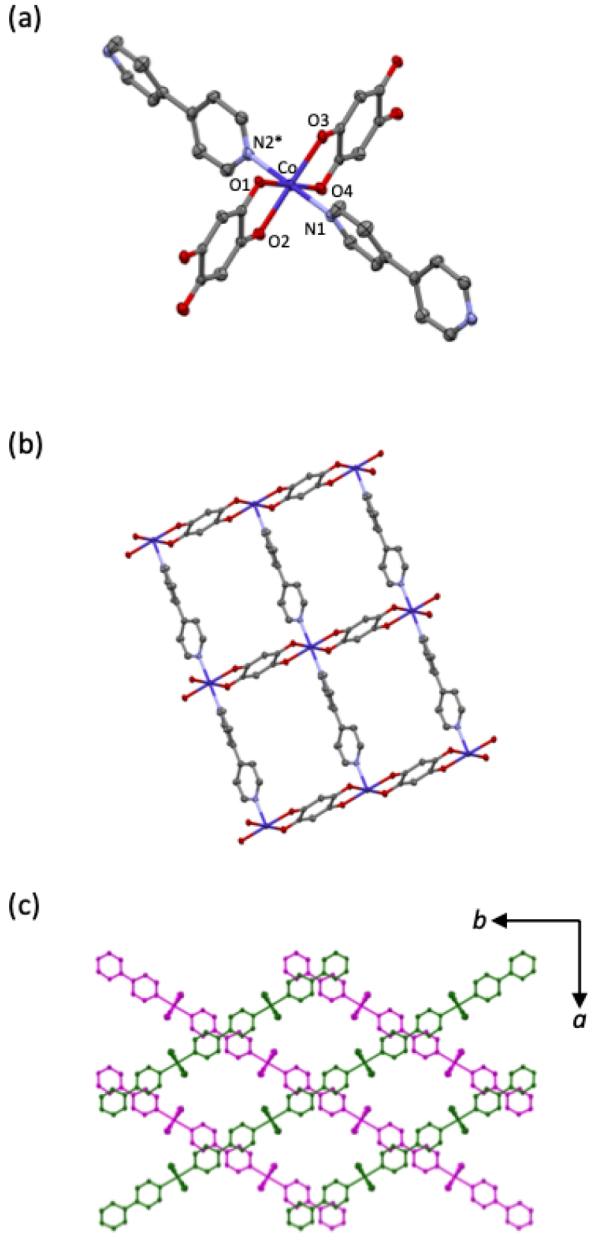

Figure 3. Structure of ***trans*-2D-Co**. The water atoms are omitted for clarity. (a) ORTEP drawing of the local structure. Perspective view of the (b) 2D net and (c) packing motif with inclined polycatenation.

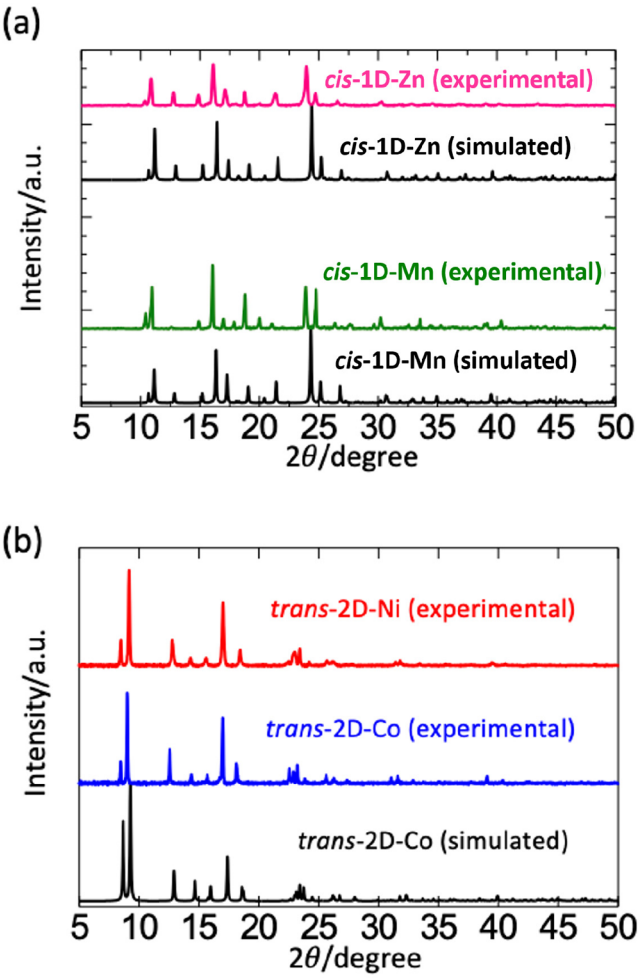

Figure 4. Powder X-ray diffraction (PXRD) patterns. (a) ***cis*-1D-Zn** and ***cis*-1D-Mn** together with a simulated pattern of ***cis*-1D-Zn** and ***cis*-1D-Mn**. (b) ***trans*-2D-Co** and ***trans*-2D-Co** together with a simulated pattern of ***trans*-2D-Co**.

trans*-2D-Cu**. The Cu−N distance is 2.0040(17) Å, whereas the Cu−O1 and Cu−O2 distances are 2.1595(17) and 2.0997(18) Å, respectively, indicating that the O1−Cu−O1* axis corresponds to the Jahn−Teller axis.[35] The other crystal structure was found only for M = Cu (Figure 5). The molar ratio of Cu, DHBQ, and bpy is 1:1:2, and the DHBQ ligands are located at the trans position to form a 1D linear chain. One side of the nitrogen atom of the bpy ligand coordinates to Cu^{2+}, whereas another side was free. Therefore, the complex is named *trans*-[Cu(DHBQ)$(bpy)_2$] (trans*-1D-Cu**). The Cu−O2 [2.235(3) Å] and Cu−O4 [2.247(3) Å] distances are significantly longer than the Cu−O1 [1.997(3) Å], Cu−O3 [1.996(3) Å], Cu−N1 [2.037(4) Å], and Cu−N2 [2.034(4) Å] distances, indicating that the O2−Cu−O4 axis is the Jahn−Teller axis.[39] The shortest C−C distance between the neighboring pyridyl ring is 3.8 Å, indicating that there is a weak $\pi-\pi$ interaction between pyridyl rings. The PXRD pattern of the Cu compound (Figure S3) was explained by the superposition of ***trans*-2D-Cu** and ***trans*-1D-Cu**.

The coordination conformation and network motifs of the crystals in relation to the metal ions is summarized in Table 1. Here, we discuss the coordination conformation in relation to the metal ions. In the case of Mn^{II} and Zn^{II}, cis conformation was formed, whereas Co^{II}, Ni^{II}, and Cu^{II} afforded trans conformation. In order to estimate the thermodynamic stability, we performed DFT calculations. The discrete neutral complexes, *cis*- or *trans*-[M(HDHBQ)$(py)_2$] (py = pyridyl), were used as model compounds to simplify the calculations. The hydration effect is considered with regards to the integral equation formalism of the polarizable continuum model (IEFPCM). The ΔG ($\equiv G_{cis} - G_{trans}$) is shown in Table 2. Our result indicates that the cis conformation is more stable, except for M = Cu. This is not consistent with the experimental result. So, we presumed that the kinetic factor plays a role for the preference. According to Shriver & Atkins's textbook, the ligand-substitution rate of the aqua complexes is in the order of $Cu^{II} > Zn^{II} > Mn^{II} > Co^{II} > Ni^{II}$,[40] which means Cu^{II} has more chance to relax to the thermodynamically stable structure before crystallization than Ni^{II} does. Meanwhile, a thermodynamically controlled crystal tends to be densely

https://doi.org/10.1021/acsomega.1c07077
ACS Omega 2022, 7, 18259−18266

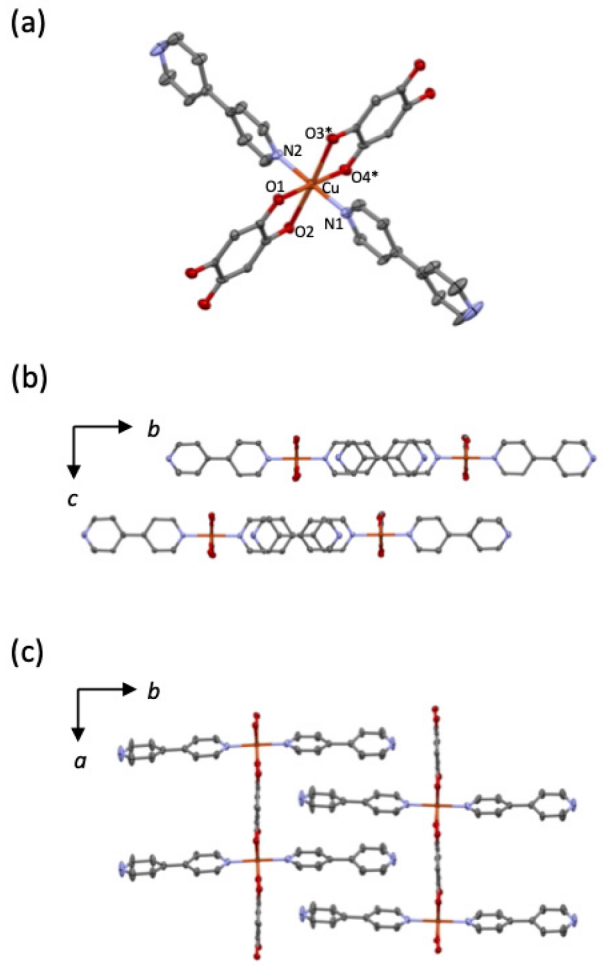

Figure 5. Structure of ***trans*-1D-Cu**. (a) ORTEP drawing of the local structure. Two perspective views along (b) *a*- and (c) *c*-axes.

Table 1. Summary of the Conformation and the Network Motifs of the Obtained Crystals

M^{II}	coordination conformation	network motif
Mn, Zn	cis	1D zigzag chain
Co, Ni	trans	3D framework (interlocking of 2D rectangular nets)
Cu	trans	mixture of 1D linear chains and 3D framework (interlocking of 2D rectangular nets), not separable

Table 2. Difference of the Gibbs Free Energies (ΔG) between cis and trans Conformers

metal	ΔG /kcal mol^{-1}[1]
Mn	−3.90467
Co	−3.84079
Ni	−0.63212
Cu	1.25780
Zn	−1.19185

[1] ΔG is defined as $\Delta G \equiv G_{cis} - G_{trans}$

packed compared to a kinetically controlled one.[41] From this point of view, because the crystal density of the cis complexes (ca. 1.6 g cm^{-3}) is higher than that of the trans complexes (ca. 1.3 g cm^{-3}), it is natural to consider that the more inert Co^{II} and Ni^{II} preferred the kinetically controlled trans conformation, whereas more labile Zn^{II} and Mn^{II} preferred the thermodynamically controlled cis conformation. In the case of Cu^{II}, the trans conformation is probably thermodynamically stable because of the Jahn−Teller effect.

Thermogravimetric analysis (TGA) of ***trans*-2D-Co** and ***trans*-2D-Ni** showed a weight decrease caused by removal of the crystal water in the pore, while ***cis*-1D-Mn** and ***cis*-1D-Zn** showed no weight loss until around 300 °C (Figure 6). The amount of water estimated from TGA is 8.7% and 10.3% for ***trans*-2D-Co** and ***trans*-2D-Ni**, respectively, which corresponds to 2.5 and 3.0 water molecules per formula unit.

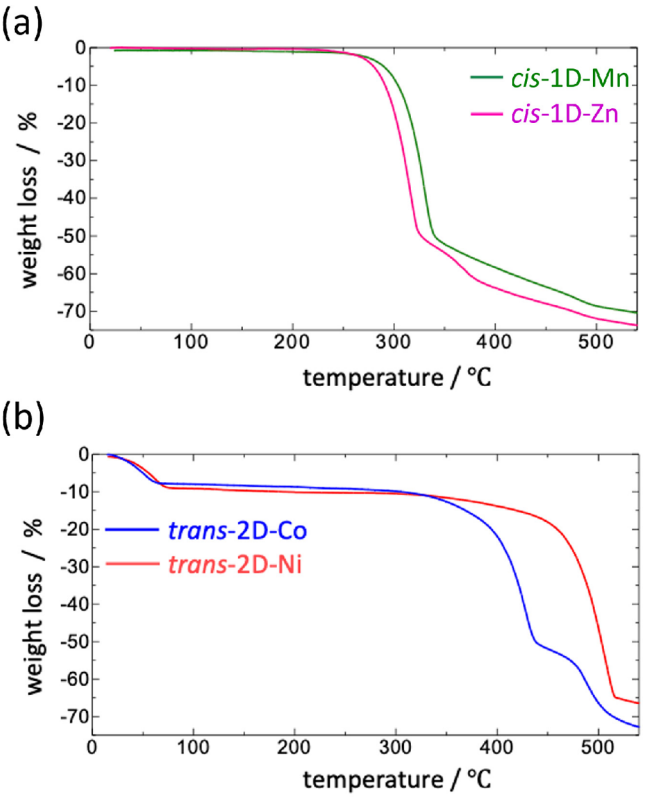

Figure 6. Thermogravimetric analysis. (a) ***cis*-1D-Zn** and ***cis*-1D-Mn**. (b) ***trans*-2D-Co** and ***trans*-2D-Ni**.

The N_2 sorption isotherms were measured to confirm the porosity of ***trans*-2D-Ni** and ***trans*-2D-Co**. (Figure 7a). The N_2 isotherms of ***trans*-2D-Ni** were classified as Type I, suggesting ***trans*-2D-Ni** has micropores. The N_2 uptake was nearly saturated at $P/P_0 = 0.9$. The further increase in the N_2 uptake at $P/P_0 > 0.95$ is probably due to adsorption on the crystalline surface. The N_2 saturated volume (ca. 60 cm^3(STP) g^{-1}) is consistent with that of the roughly estimated volume (74.7 cm^3(STP) g^{-1}) from the crystal structure (see details in SI). The BET and Langmuir surface areas of ***trans*-2D-Ni** were estimated to be 177 and 183 m^2g^{-1}, respectively. However, ***trans*-2D-Co** showed almost no N_2 uptake despite its porous structure. As for the H_2 adsorption (Figure 7b), the Ni and Co compounds showed 90 and 20 cm^3(STP) g^{-1}, respectively, at 77 K and 1 atm. It is noteworthy that both compounds showed larger H_2 uptake than N_2 at 77 K and 1 atm. In particular, ***trans*-2D-Co** showed almost no N_2 uptake, but moderate H_2 uptake. Such a phenomenon is not common because the boiling point of N_2 (77 K) is much higher than H_2 (20 K), but it is reported in several MOFs with quite small pores.[42,43] In

https://doi.org/10.1021/acsomega.1c07077
ACS Omega 2022, 7, 18259−18266

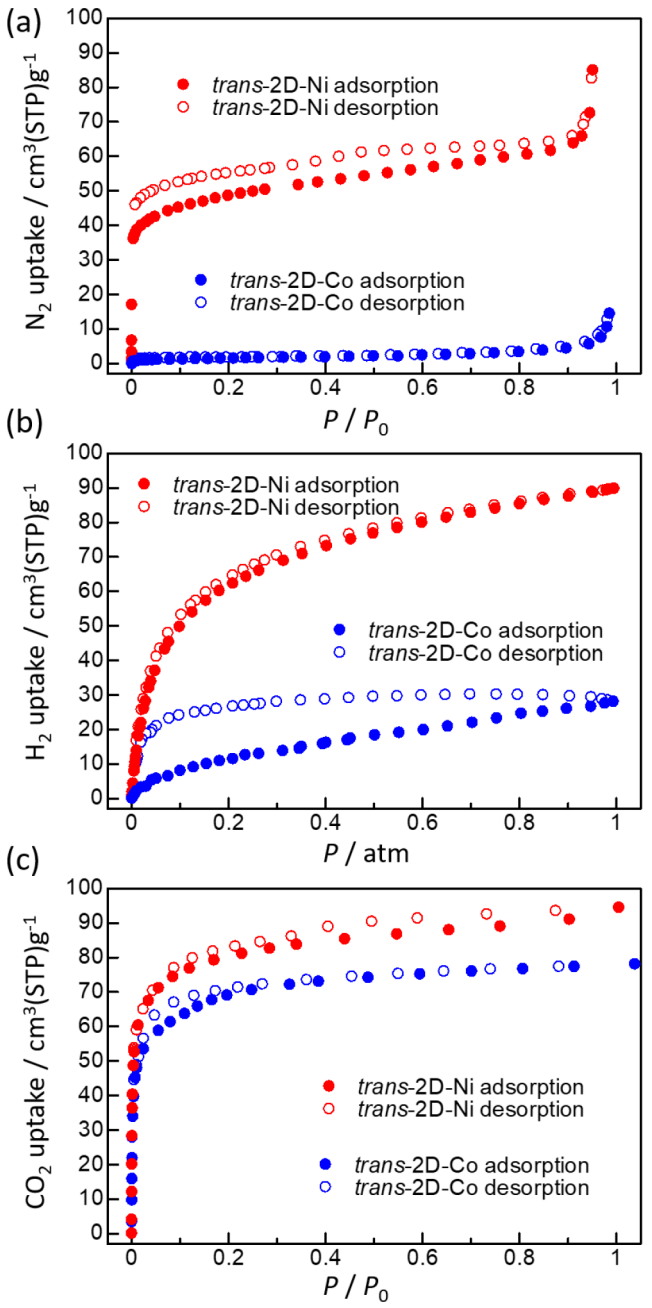

Figure 7. (a) N_2 adsorption isotherms at 77 K, (b) H_2 adsorption isotherms at 77 K, and (c) CO_2 adsorption isotherms at 195 K in ***trans*-2D-Co** and ***trans*-2D-Ni**.

these MOFs, only H_2 can enter the pore because H_2 has a smaller kinetic diameter (2.89 Å) than N_2 (3.64 Å).[44] Therefore, we presume that the unusual N_2 and H_2 uptake phenomenon is due to the small 1D pore of the present compounds. This presumption is supported by the hysteresis of the H_2 isotherm observed in ***trans*-2D-Co**. Such a hysteresis is often observed when the kinetics of the adsorption are quite slow because of the slow diffusion in the small pores.

Here, we discuss the origin of the difference in the sorption properties between ***trans*-2D-Co** and ***trans*-2D-Ni**. Figure S10 shows scanning electron microscope (SEM) images of both compounds. ***trans*-2D-Co** crystals were needle shaped with a typical length of 10−30 μm, and we confirmed that the long axis of the crystal is parallel to the 1D pore by using SXRD measurement. Conversely, the crystal particle of ***trans*-2D-Ni** is much smaller than ***trans*-2D-Co** and typically 1 μm size. Therefore, in the case of ***trans*-2D-Co**, the adsorbent molecules have to diffuse a longer distance to reach the center of the crystal particle. This is one of the possible reasons for the difference. Another possible reason is in the flexibility of the framework. As we noted above, the framework of ***trans*-2D-Co** can be more flexible than that of ***trans*-2D-Ni**. Therefore, the structural change by the removal of solvent molecules should be larger in ***trans*-2D-Co**, which affords smaller pore size.

Such a diffusion issue is less dominant at higher temperature because of the greater lattice motion. Thus, we performed CO_2 adsorption at 195 K. As a result, both compounds showed similar isotherms, as expected (Figure 7c). Therefore, we concluded that the difference in the adsorption isotherms between ***trans*-2D-Co** and ***trans*-2D-Ni** is due to the difference of the crystal shape or subtle differences in the pore structure, both of which affect large diffusion kinetics.

Figure 8 shows the UV−vis−NIR spectra of ***cis*-1D-M** and ***trans*-2D-M**, which is evaluated by the Kubelka−Munk

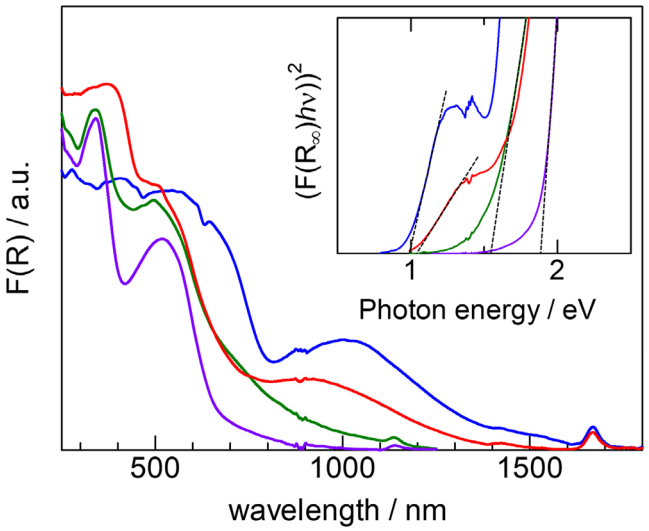

Figure 8. UV−vis−NIR spectra of ***cis*-1D-M** and ***trans*-2D-M**. Inset shows Tauc plot by assuming the indirect band gap.

transformation of the raw diffuse reflectance spectra. The UV−vis−NIR spectrum of ***cis*-1D-M** shows mainly two bands at 360 and 520 nm. On the basis of the assignment of the spectrum in $(H_2NMe_2)_{1.5}Cr_2(DHBQ)_3$,[45] we assigned these bands to a ligand-based $\pi^*-\pi^*$ and $\pi-\pi^*$ transition, respectively. Alternatively, the UV−vis−NIR spectra of ***trans*-2D-M** exhibits three bands around 440, 600, and 1000 nm. The two higher energy transitions are assigned as a d−d transition involving a ligand-based $\pi^*-\pi^*$ and $\pi-\pi^*$ transition, respectively. The broad peak in the mid-IR region is assigned as a ligand-to-metal charge transfer (LMCT) or metal-to-ligand charge transfer (MLCT). The sharp absorbances around 1160 and 1680 nm are probably due to overtones of contaminating water. By assuming the indirect band gap, we showed the Tacu plot in the inset of Figure 8. The optical band gaps of ***cis*-1D-Mn**, ***cis*-1D-Zn**, ***trans*-2D-Co**, and ***trans*-2D-Ni** were estimated to be 1.6, 1.8, 1.0, and 1.1 eV, respectively.

https://doi.org/10.1021/acsomega.1c07077
ACS Omega 2022, 7, 18259−18266

CONCLUSION

In conclusion, the binary DHBQ-based CPs, *cis*-[M(DHBQ)-$(bpy)_2$] (M = Mn and Zn), *trans*-[M(DHBQ)(bpy)] (M = Co, Ni, and Cu), and *trans*-[Cu(DHBQ)$(bpy)_2$] were synthesized using *in situ* hydrolysis of a DMBQ precursor. These were characterized with SXRD, PXRD, IR, TGA, H_2, N_2, and CO_2 adsorption; magnetic susceptibility; and elemental analysis. This *in situ* hydrolysis method is beneficial not only to grow a good, single crystal but also to introduce auxiliary ligands into an MOF, which leads to the diversity of MOFs. Thus, the present synthetic approach should lead to the further application of redox-active MOFs, such as cathode materials of secondary batteries, electrode catalysts, etc.

ASSOCIATED CONTENT

Supporting Information

The Supporting Information is available free of charge at https://pubs.acs.org/doi/10.1021/acsomega.1c07077.

Details of experimental methods and crystallographic and spectral information (PDF)

AUTHOR INFORMATION

Corresponding Author

Shinya Takaishi − *Department of Chemistry, Graduate School of Science, Tohoku University, Sendai, Miyagi 980-8578, Japan*; orcid.org/0000-0002-6739-8119; Email: shinya.takaishi.d8@tohoku.ac.jp

Authors

Daiki Yamazui − *Department of Chemistry, Graduate School of Science, Tohoku University, Sendai, Miyagi 980-8578, Japan*

Kaiji Uchida − *Department of Chemistry, Graduate School of Science, Tohoku University, Sendai, Miyagi 980-8578, Japan*

Shohei Koyama − *Department of Chemistry, Graduate School of Science, Tohoku University, Sendai, Miyagi 980-8578, Japan*; orcid.org/0000-0003-3164-8443

Bin Wu − *Department of Chemistry, Graduate School of Science, Tohoku University, Sendai, Miyagi 980-8578, Japan*

Hiroaki Iguchi − *Department of Chemistry, Graduate School of Science, Tohoku University, Sendai, Miyagi 980-8578, Japan*; orcid.org/0000-0001-5368-3157

Wataru Kosaka − *Institute for Materials Research, Tohoku University, Sendai 980-8577, Japan*; orcid.org/0000-0002-2445-5099

Hitoshi Miyasaka − *Institute for Materials Research, Tohoku University, Sendai 980-8577, Japan*; orcid.org/0000-0001-9897-0782

Complete contact information is available at: https://pubs.acs.org/10.1021/acsomega.1c07077

Notes

The authors declare no competing financial interest.

CCDC 2080443, 2080444, 2080445, 2080447, 2106002, and 2151004 contain the supplementary crystallographic data for this paper. These data can be obtained free of charge via www.ccdc.cam.ac.uk/data_request/cif, by emailing data_request@ccdc.cam.ac.uk, by contacting The Cambridge Crystallographic Data Centre at 12 Union Road, Cambridge CB2 1EZ, UK; fax, + 44 1223 336033.

ACKNOWLEDGMENTS

This work was partially supported by a JSPS KAKENHI Grant (B) 19H02729 and Grant (A) 21H04696 and by the Tohoku University Molecule & Material Synthesis Plat-Form in Nanotechnology Platform Project sponsored by the Ministry of Education, Culture, Sports, Science and Technology (MEXT), Japan.

REFERENCES

(1) Schoedel, A.; Ji, Z.; Yaghi, O. M. The role of metal-organic frameworks in a carbon-neutral energy cycle. *Nature Energy* **2016**, *1*, 16034.

(2) Suh, M. P.; Park, H. J.; Prasad, T. K.; Lim, D.-W. Hydrogen Storage in Metal-Organic Frameworks. *Chem. Rev.* **2012**, *112*, 782−835.

(3) Rowsell, J. L. C.; Yaghi, O. M. Strategies for Hydrogen Storage in Metal-Organic Frameworks. *Angew. Chem., Int. Ed.* **2005**, *44*, 4670−4679.

(4) Sumida, K.; Rogow, D. L.; Mason, J. A.; McDonald, T. M.; Bloch, E. D.; Herm, Z. R.; Bae, T.-H.; Long, J. R. Carbon Dioxide Capture in Metal-Organic Frameworks. *Chem. Rev.* **2012**, *112*, 724−781.

(5) Millward, A. R.; Yaghi, O. M. Metal−Organic Frameworks with Exceptionally High Capacity for Storage of Carbon Dioxide at Room Temperature. *J. Am. Chem. Soc.* **2005**, *127*, 17998−17999.

(6) Peng, Y.; Krungleviciute, V.; Eryazici, I.; Hupp, J. T.; Farha, O. K.; Yildirim, T. Methane Storage in Metal-Organic Frameworks: Current Records, Surprise Findings, and Challenges. *J. Am. Chem. Soc.* **2013**, *135*, 11887−11894.

(7) Matsuda, R.; Kitaura, R.; Kitagawa, S.; Kubota, Y.; Belosludov, R. V.; Kobayashi, T. C.; Sakamoto, H.; Chiba, T.; Takata, M.; Kawazoe, Y.; Mita, Y. Highly controlled acetylene accommodation in a metal-organic microporous material. *Nature* **2005**, *436*, 238−241.

(8) Li, J. R.; Sculley, J.; Zhou, H.-C. Metal-Organic Frameworks for Separations. *Chem. Rev.* **2012**, *112*, 869−932.

(9) Duan, J.; Higuchi, M.; Krishna, R.; Kiyonaga, T.; Tsutsumi, Y.; Sato, Y.; Kubota, Y.; Takata, M.; Kitagawa, S. High $CO_2/N_2/O_2/CO$ separation in a chemically robust porous coordination polymer with low binding energy. *Chem. Sci.* **2014**, *5*, 660−666.

(10) Ma, S.; Wang, X.-S.; Yuan, D.; Zhou, H.-C. A coordinatively linked Yb metal-organic framework demonstrates high thermal stability and uncommon gas-adsorption selectivity. *Angew. Chem., Int. Ed.* **2008**, *47*, 4130−4133.

(11) Dincă, M.; Long, J. R. Strong H2 Binding and Selective Gas Adsorption within the Microporous Coordination Solid $Mg_3(O_2C\text{-}C_{10}H_6\text{-}CO_2)_3$. *J. Am. Chem. Soc.* **2005**, *127*, 9376−9377.

(12) Kreno, L. E.; Leong, K.; Farha, O. K.; Allendorf, M.; Van Duyne, R. P.; Hupp, J. T. Metal-Organic Framework Materials as Chemical Sensors. *Chem. Rev.* **2012**, *112*, 1105−1125.

(13) Lee, J.; Farha, O. K.; Roberts, J.; Scheidt, K. A.; Nguyen, S. T.; Hupp, J. T. Metal-organic framework materials as catalysts. *Chem. Soc. Rev.* **2009**, *38*, 1450−1459.

(14) Ma, L.; Abney, C.; Lin, W. Enantioselective catalysis with homochiral metal-organic frameworks. *Chem. Soc. Rev.* **2009**, *38*, 1248−1256.

(15) Yoon, M.; Srirambalaji, R.; Kim, K. Homochiral Metal-Organic Frameworks for Asymmetric Heterogeneous Catalysis. *Chem. Rev.* **2012**, *112*, 1196−1231.

(16) Jeon, I.; Negru, B.; Van Duyne, R.; Harris, T. A 2D Semiquinone Radical-Containing Microporous Magnet with Solvent-Induced Switching from T_c = 26 to 80 K. *J. Am. Chem. Soc.* **2015**, *137* (50), 15699−15702.

(17) DeGayner, J.; Jeon, I.; Sun, L.; Dinca, M.; Harris, T. 2D Conductive Iron-Quinoid Magnets Ordering up to T_c = 105 K via Heterogenous Redox Chemistry. *J. Am. Chem. Soc.* **2017**, *139* (11), 4175−4184.

(18) Chen, J.; Sekine, Y.; Komatsumaru, Y.; Hayami, S.; Miyasaka, H. Thermally Induced Valence Tautomeric Transition in a Two-

Dimensional Fe-Tetraoxolene Honeycomb Network. *Angew. Chem., Int. Ed.* **2018**, *57* (37), 12043−12047.
(19) Darago, L. E.; Aubrey, M. L.; Yu, C. J.; Gonzalez, M. I.; Long, J. R. Electronic Conductivity, Ferrimagnetic Ordering, and Reductive Insertion Mediated by Organic Mixed-Valence in a Ferric Semiquinoid Metal-Organic Framework. *J. Am. Chem. Soc.* **2015**, *137* (50), 15703−15711.
(20) Ziebel, M. E.; Darago, L. E.; Long, J. R. Control of Electronic Structure and Conductivity in Two-Dimensional Metal-Semiquinoid Frameworks of Titanium, Vanadium, and Chromium. *J. Am. Chem. Soc.* **2018**, *140* (8), 3040−3051.
(21) Ziebel, M. E.; Gaggioli, C. A.; Turkiewicz, A. B.; Ryu, W.; Gagliardi, L.; Long, J. R. Effects of Covalency on Anionic Redox Chemistry in Semiquinoid Based Metal−Organic Frameworks. *J. Am. Chem. Soc.* **2020**, *142*, 2653−2664.
(22) Yamada, T.; Morikawa, S.; Kitagawa, H. Structures and Proton Conductivity of One-Dimensional M(Dhbq)·n H_2O (M = Mg, Mn, Co, Ni, and Zn, H2(Dhbq) = 2,5-Dihydroxy-1,4-Benzoquinone) Promoted by Connected Hydrogen-Bond Networks with Absorbed Water. *Bull. Chem. Soc. Jpn.* **2010**, *83* (1), 42−48.
(23) Abrahams, B. F.; Hudson, T. A.; McCormick, L. J.; Robson, R. Coordination Polymers of 2,5-Dihydroxybenzoquinone and Chloranilic Acid with the (10,3)- A Topology. *Cryst. Growth Des.* **2011**, *11* (7), 2717−2720.
(24) Kitagawa, S.; Kawata, S. Coordination Compounds of 1,4-Dihydroxybenzoquinone and Its Homologues. Structures and Properties. *Coord. Chem. Rev.* **2002**, *224* (1−2), 11−34.
(25) Kawata, S.; Kitagawa, S.; Kumagai, H.; Kudo, C.; Kamesaki, H.; Ishiyama, T.; Suzuki, R.; Kondo, M.; Katada, M. Rational design of a novel intercalation system. Layer-gap control of crystalline coordination polymers, $\{[Cu(CA)(H_2O)_m](G)\}_n$ (m = 2,G = 2,5-dimethylpyrazine and phenazine; m = 1, G = **1**, 2, 3, 4, 6, 7, 8, 9-octahydrophenazine). *Inorg. Chem.* **1996**, *35* (15), 4449−4461.
(26) Kabir, M.; Kawahara, M.; Kumagai, H.; Adachi, K.; Kawata, S.; Ishii, T.; Kitagawa, S. The rational syntheses of manganese-chloranilate compounds: crystal structures and magnetic properties. *Polyhedron* **2001**, *20* (11−14), 1417−1422.
(27) Frisch, M. J.; Trucks, G. W.; Schlegel, H. B.; Scuseria, G. E.; Robb, M. A.; Cheeseman, J. R.; Scalmani, G.; Barone, V.; Petersson, G. A.; Nakatsuji, H.; Li, X.; Caricato, M.; Marenich, A. V.; Bloino, J.; Janesko, B. G.; Gomperts, R.; Mennucci, B.; Hratchian, H. P.; Ortiz, J. V.; Izmaylov, A. F.; Sonnenberg, J. L.; Williams-Young, D.; Ding, F.; Lipparini, F.; Egidi, F.; Goings, J.; Peng, B.; Petrone, A.; Henderson, T.; Ranasinghe, D.; Zakrzewski, V. G.; Gao, J.; Rega, N.; Zheng, G.; Liang, W.; Hada, M.; Ehara, M.; Toyota, K.; Fukuda, R.; Hasegawa, J.; Ishida, M.; Nakajima, T.; Honda, Y.; Kitao, O.; Nakai, H.; Vreven, T.; Throssell, K.; Montgomery, J. A., Jr.; Peralta, J. E.; Ogliaro, F.; Bearpark, M. J.; Heyd, J. J.; Brothers, E. N.; Kudin, K. N.; Staroverov, V. N.; Keith, T. A.; Kobayashi, R.; Normand, J.; Raghavachari, K.; Rendell, A. P.; Burant, J. C.; Iyengar, S. S.; Tomasi, J.; Cossi, M.; Millam, J. M.; Klene, M.; Adamo, C.; Cammi, R.; Ochterski, J. W.; Martin, R. L.; Morokuma, K.; Farkas, O.; Foresman, J. B.; Fox, D. J. *Gaussian 16, Revision C.01*; Gaussian, Inc.: Wallingford, CT, 2016.
(28) Becke, A. D. Density-Functional Thermochemistry. III. The Role of Exact Exchange. *J. Chem. Phys.* **1993**, *98* (7), 5648−5652.
(29) Lee, C.; Yang, W.; Parr, R. G. Development of the Colle-Salvetti Correlation-Energy Formula into a Functional of the Electron Density. *Phys. Rev. B* **1988**, *37* (2), 785−789.
(30) Frisch, M. J.; Pople, J. A.; Binkley, J. S. Self-Consistent Molecular Orbital Methods 25. Supplementary Functions for Gaussian Basis Sets. *J. Chem. Phys.* **1984**, *80* (7), 3265−3269.
(31) Tao, Y.; Pang, X.-H.; Li, H.-Y.; Bian, H.-D.; Liu, H.-F.; Huang, F.-P. In Situ Metal-Ligand Reactions under Solvent-Dependent Hydro(solvo)thermal Conditions: Structures, Mass Spectrometry, and Magnetism. *Inorg. Chem.* **2020**, *59*, 308−314.
(32) Kong, X.; Hu, K.; Wu, Q.; Mei, L.; Yu, J.; Chai, Z.; Nie, C.; Shi, W. In situ nitroso formation induced structural diversity of uranyl coordination polymers. *Inorg. Chem. Frontiers* **2019**, *6* (3), 775−785.
(33) Sheldrick, G. M. Crystal structure refinement with SHELXL. *Acta Crystallogr. C* **2015**, *71*, 3−8.
(34) Gan, X.; Jiang, W.; Wang, W.; Hu, L. An Approach to 3,6-Disubstituted 2,5-Dioxybenzoquinones via Two Sequential Suzuki Couplings. Three-Step Synthesis of Leucomelone. *Org. Lett.* **2009**, *11* (3), 589−592.
(35) Deguenon, D.; Bernardinelli, G.; Tuchagues, J.; Castan, P. Molecular-crystal structure and magnetic -properties of (croconato)-manganese(II) and (oxalato)manganese(II) complexes. *Inorg. Chem.* **1990**, *29* (16), 3031−3037.
(36) Liu, L.; DeGayner, J.; Sun, L.; Zee, D.; Harris, T. Reversible redox switching of magnetic order and electrical conductivity in a 2D manganese benzoquinoid framework. *Chem. Sci.* **2019**, *10* (17), 4652−4661.
(37) Carlucci, L.; Ciani, G.; Proserpio, D. Polycatenation, polythreading and polyknotting in coordination network chemistry. *Coord. Chem. Rev.* **2003**, *246* (1−2), 247−289.
(38) De Munno, G.; Julve, M.; Lloret, F.; Faus, J.; Caneschi, A. 2,2'-Bipyrimidiene (bipym)-bridged dinuclear complexes Part 4. Synthesis, crystal-structure and magnetic-properties of $[Co_2(H_2O)_8(bipym)][NO_3]_4$, $[Co_2(H_2O)_8(bipym)][SO_4]_2\cdot 2H_2O$ and $[Co_2(bipym)_3(NCS)_4]$. *J. Chem. Soc., Dalton Trans.* **1994**, No. 8, 1175−1183.
(39) Jahn, H.; Teller, E. Stability of Polyatomic Molecules in Degenerate Electronic States. I. Orbital Degeneracy. *Proc. Royal Soc. London A* **1937**, *161* (905), 220−235.
(40) Atkins, P.; Overton, T.; Rourke, J.; Weller, M.; Armstrong, F. *Shriver & Atkins' Inorganic Chemistry*, 5th ed.; Oxford University Press, 2009; p 508.
(41) Ohtsu, H.; Kawano, M. Kinetic assembly of coordination networks. *Chem. Commun.* **2017**, *53* (63), 8818−8829.
(42) Dincă, M.; Long, J. R. Strong H_2 binding and selective gas adsorption within the microporous Microporous Coordination Solid $Mg_3(O_2C\text{-}C_{10}H_6\text{-}CO_2)_3$. *J. Am. Chem. Soc.* **2005**, *127*, 9376−9377.
(43) Dybtsev, D.; Chun, H.; Yoon, S.; Kim, D.; Kim, K. Microporous manganese formate: A simple metal-organic porous material with high framework stability and highly selective gas sorption properties. *J. Am. Chem. Soc.* **2004**, *126* (1), 32−33.
(44) Breck, D. W. *Zeolite Molecular Sieves*; Wiley & Sons: New York, 1974.
(45) Ziebel, M. E.; Darago, L. E.; Long, J. R. Control of Electronic Structure and Conductivity in Two-Dimensional Metal-Semiquinoid Frameworks of Titanium, Vanadium, and Chromium. *J. Am. Chem. Soc.* **2018**, *140* (8), 3040−3051.

https://doi.org/10.1021/acsomega.1c07077
ACS Omega 2022, 7, 18259−18266